HVEM high-temperature in situ straining experiments on cubic zirconia single crystals

D. Baither *, B. Baufeld, U. Messerschmidt, M. Bartsch

Max-Planck-Institut für Mikrostrukturphysik, Weinberg 2, D-06120 Halle (Saale), Germany

Abstract

Cubic ZrO_2 single crystals fully stabilized with 9.4 mol% Y_2O_3 were strained in situ in a high-temperature tensile straining stage inside a high-voltage electron microscope. Straining was usually performed at 1150°C. One experiment started at 1150°C was interrupted before it was continued at 870°C. For investigating the dependence of the deformation process on the activated slip systems, specimens with $\langle 112 \rangle$ and $\langle 100 \rangle$ tensile axes were used. Specimens with a $\langle 112 \rangle$ tensile axis, where single slip on one cube slip system is preferentially activated, were prepared to have $\{111\}$ or $\{110\}$ foil surfaces. Of the specimens with a $\langle 100 \rangle$ tensile axis, where slip on cube planes is suppressed, $\{001\}$ foil surfaces were chosen. The observed dislocation structures and especially the dynamic behaviour of dislocations recorded on video tape furnished information on the mode of dislocation multiplication and on the mechanisms controlling the flow stress. The analyses of the dislocation density provided a value of the long-range stress component. Estimating the local shear stress from the bowed-out dislocation segments yielded a semi-quantitative explanation of the macroscopic flow stress for the deformation on the cube slip plane at 1150°C. In this temperature range, the athermal dislocation motion is in accordance with the very low strain rate sensitivity measured in macroscopic tests. At 870°C, dislocations are pinned at localized obstacles. Dislocations on non-cube systems experience a lattice friction, even at 1150°C. © 1997 Elsevier Science S.A.

Keywords: Cubic zirconia single crystals; High-voltage electron microscope; Straining

1. Introduction

Cubic ZrO_2 has been intensively investigated, in particular as a model substance of the matrix of two-phase zirconia (partially stabilized zirconia, PSZ), or zirconia-containing ceramics, which are prospective materials for high-temperature applications. Extensive macroscopic deformation tests were performed in a wide temperature range above 1000°C [1–4]. These experiments were extended to temperatures down to 400°C without confining hydrostatic pressure, where zirconia was considered a very brittle material [5–7]. In spite of these numerous investigations, the mechanisms controlling the flow stress are not satisfactorily understood. A serious problem arises from the relaxation and recovery of the dislocation structures observed after the macroscopic tests, even if the specimens are cooled under load. Moreover, information on the kinetics of individual dislocations is almost not available. High-temperature in situ straining experiments in a transmission electron microscope may avoid some of these problems enabling a deeper insight into the microprocesses of deformation [8]. At temperatures near or somewhat above 1000°C, strain rate change and stress relaxation tests during macroscopic deformation revealed a very low strain rate sensitivity, indicating an almost athermal deformation behaviour [5–7]. Below 1000°C, however, thermally activated processes were observed again, which are associated with local pinning of the dislocations [5–7,9]. Thus, in situ experiments in a high-voltage electron microscope (HVEM) described in the present paper were performed in a temperature range which was experimentally feasible, i.e., between 870 and 1150°C.

* Corresponding author. Tel.: +49 345 558250; fax: +49 345 5511223; e-mail: baither@secundus.mpi-msp-halle.mpg.de.

2. Experimental

ZrO$_2$ single crystals with 9.4 mol% Y$_2$O$_3$, prepared by the skull melting technique, were obtained from the Ceres Corporation, North Billerica, MA, USA. The in situ experiments in the tensile straining stage of the HVEM require samples of 8 mm length and about 2 mm width. The sample is fastened to the grips of the straining stage by two 0.5 mm tungsten pins located 5 mm apart.

At first, slices about 0.3 mm thick were cut by a wire saw from a parallelepiped with faces well oriented corresponding to the desired straining direction and foil surface, described below. After drilling the holes by an ultrasonic drilling machine, the samples were ground to a thickness of 0.1 mm on a brass plate, using a 3 μm diamond suspension, and subsequently polished with the same suspension on a polishing cloth. The central region of the sample was then further thinned by a dimple grinder, especially to obtain a cross section of the specimen which is small enough to enable deformation at the limited force of the stage. The final thinning down to a thickness of 0.5 μm of the central region was performed in an argon ion mill. For the in situ specimens of this brittle material, it is essential to polish all faces carefully and to avoid perforation in the central region so as to prevent fracture.

The in situ experiments were carried out in a specially designed double-tilting straining stage at 1150 or 870°C in an HVEM (JEM 1000) at an acceleration voltage of 1000 kV. This stage was described in detail elsewhere [10]. In addition to micrographs of the dislocation structure on photographic films, a video system

could be used to record the dislocation motion. Usually, the straining was stopped before fracture and the details of the dislocation structure formed under load were investigated post mortem at room temperature (RT) in a wide-angle goniometer.

3. Results

3.1. Deformation in ⟨112⟩ direction

The specimen geometry for straining in [$\bar{1}1\bar{2}$] direction is outlined in Fig. 1. Usually a ($\bar{1}11$) surface of the sample was chosen, except in one case where a (110) surface was used. In [$\bar{1}1\bar{2}$] deformation direction, single slip on the [$1\bar{1}0$](001) system is favoured, with the orientation factor being 0.47. Other glide systems possible having relatively large orientation factors are [101]($11\bar{1}$), [$01\bar{1}$](111) with 0.41 (Fig. 1(a)) and [$01\bar{1}$](100), [101](010) with 0.35 (Fig. 1(b)), respectively.

3.1.1. Deformation at 1150°C

3.1.1.1. Dislocation structure. In all deformed samples with ($\bar{1}11$) foil surfaces, the dislocations nucleated, almost without exception, on the [$1\bar{1}0$](001) slip system, which in the following will be called the primary system. Dislocations or half-loops of distinctive edge character were observed (marked by E in Fig. 2), rarely screw dislocations (S), and particularly *alpha-shaped* dislocation configurations (A). These alpha-shaped configurations always consist of a straight screw segment and a more or less bowed edge one. Large-angle tilt experiments and stereo pairs of micrographs (Fig. 3) reveal that they mostly exhibit a helical structure instead of a single large jog. In addition, a large number of dislocation loops occur. The larger ones mainly extend on the (001) slip plane. With decreasing diameter, their habit planes deviate more from the slip plane towards ($\bar{1}11$) planes parallel to the foil surface. The larger loops, in particular, show relatively straight ⟨100⟩-oriented segments, distinctly visible in Fig. 3. In several cases, single bands of long edge dislocations occur (Fig. 2(a)). Like the other dislocations, these elongated edge dislocations are arranged on (001) planes, usually having a 1/2[$1\bar{1}0$] Burgers vector. Occasionally, however, inside the edge dislocation bands there were a few dislocations with other Burgers vectors of 1/2⟨110⟩ type, which are imaged in Fig. 2(b).

The dislocation structure of the sample with (110) foil surfaces, presented as the front faces in Fig. 1, is quite different. In contrast to the previous case, here the (001) slip plane is oriented edge on, and the 1/2[$1\bar{1}0$] Burgers vector is parallel to the surface. Thus, the straight edge dislocations appear as short projections (E in Fig. 4(a)) and become well visible only if the sample
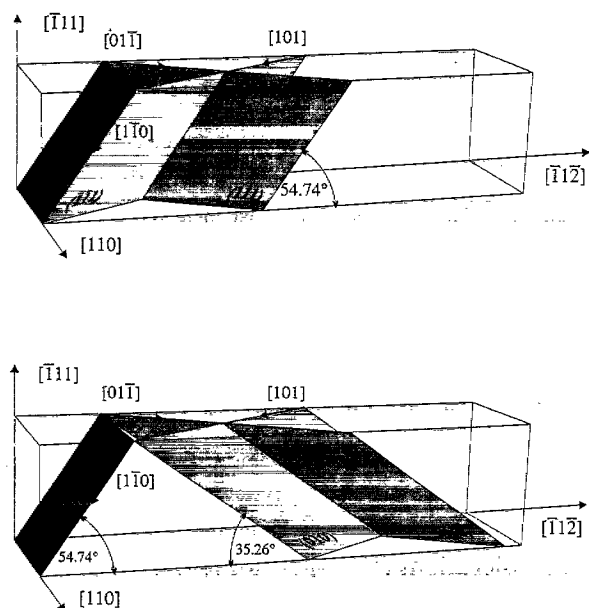

Fig. 1. Schematic drawing of the specimen and slip geometry at deformation in [$1\bar{1}2$] direction.
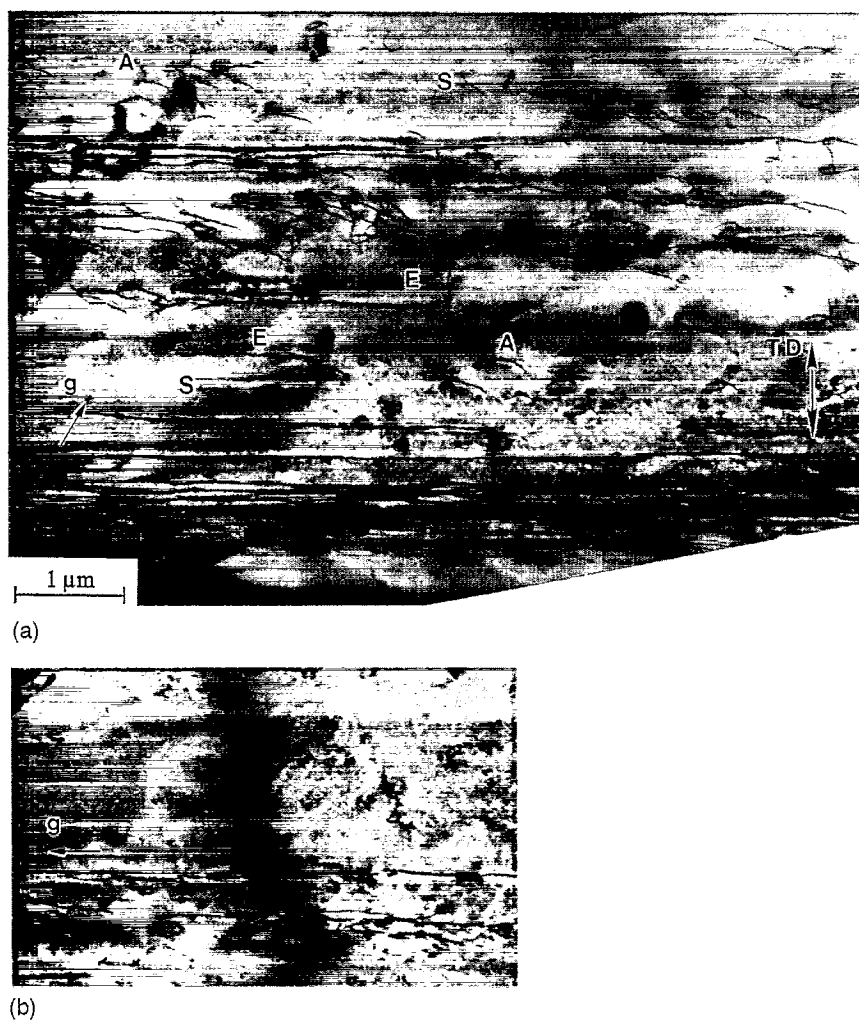
Fig. 2. Dislocation structure in a sample with $(\bar{1}11)$ foil surfaces during in situ straining in $[1\bar{1}2]$ direction (TD) imaged with different $\vec{g}$ vectors. E, edge dislocation; S, screw dislocation; A, alpha-shaped dislocation configuration. (a) $\vec{g} = [202]$; (b) $\vec{g} = [220]$, dislocations of the primary system are invisible.

is tilted by a larger angle (Fig. 4(b)). Dislocation segments of the $[1\bar{1}0](001)$ slip system with line directions deviating from the edge orientation were very exceptional. However, in addition, dislocations of a second slip system with a $1/2[0\bar{1}1]$ Burgers vector were dominant. Besides relatively elongated straight segments of this type in screw orientation, very often half-loops or segments of helical shape appeared, which were pinned at the primary edge dislocations (H in Fig. 4). A careful microscopic analysis revealed that these curved segments lie on or near the (211) plane. Unfortunately, it was not possible to bring this plane into edge-on orientation at the given foil normal. However, micrographs taken at the $[22\bar{3}]$ (Fig. 5) and [223] poles demonstrate the occurrence of this unexpected slip plane. In the inset of Fig. 5, the projection of a circular dislocation loop on a (211) plane is schematically drawn in comparison to the (011) and (111) planes usually considered. Besides the tilt analysis, the slip direction inferred from

the points where the gliding dislocations penetrate the surface confirms the above result, as will be described in the next section.

In addition to the dislocations of both the dominating slip systems mentioned above, a few dislocations with other Burgers vectors of the type $1/2\langle 110 \rangle$ were observed, partly as reaction products.

3.1.1.2. Dislocation dynamics. In samples with $(\bar{1}11)$ surfaces, dislocations are created instantaneously in a region larger than the area under observation of about 15 μm in diameter, i.e., it was impossible to analyse their formation. The dislocations move very jerkily at jump distances usually larger than the viewing area. The video recordings mostly show only the appearance or disappearance of dislocations and dislocation loops, with the slip of individual segments only rarely recorded in subsequent video frames. Examples are given in the video sequences of Figs. 6 and 7. The
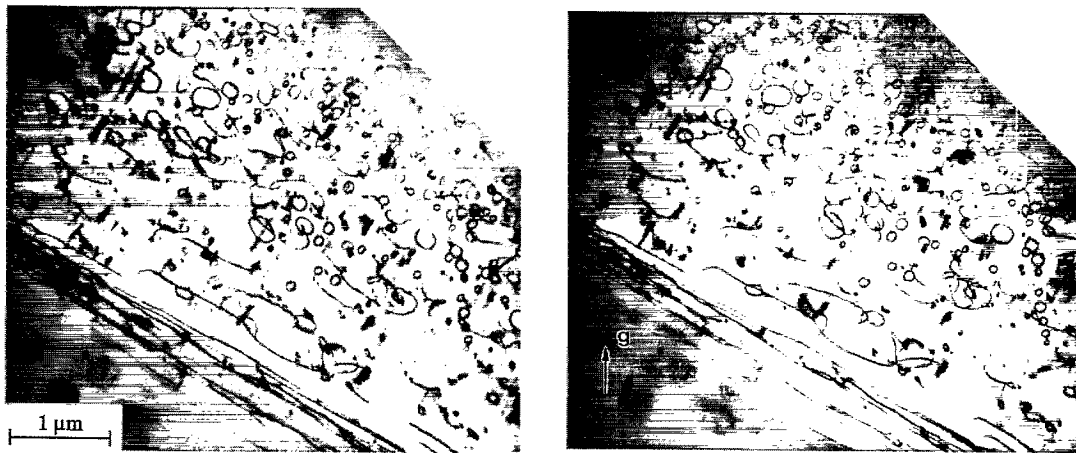
Fig. 3. Stereo pair of post mortem micrographs of the sample shown in Fig. 2.

dislocation loop L in Fig. 6(a) already had disappeared in the subsequent video frame, i.e., within 0.04 s. For the dislocation loop marked by the arrow, several stages were recorded in Fig. 6(a)–(d) taken after intervals of about 1 s. From (a) to (b), the loop expands, whereas in (c) it partly escapes to the surface. The remaining segments are anchored at a large jog, dis-

tinctly visible at the loop in Fig. 6(b). The jog can glide to the surface in the direction of the Burgers vector with the dislocation getting glissile and moving away, from (c) to (d). A very striking example is presented in Fig. 7, with the jump of a dislocation proceeding within the viewing area. Dislocation D appears within 0.04 s between Fig. 7(a) and (b), remains nearly 2 s in its position before it jumps within 0.04 s to the next one in Fig. 7(c). From this jump distance of about 2 μm one can estimate a lower limit of the velocity of 50 μm s^{-1} during the jumps.
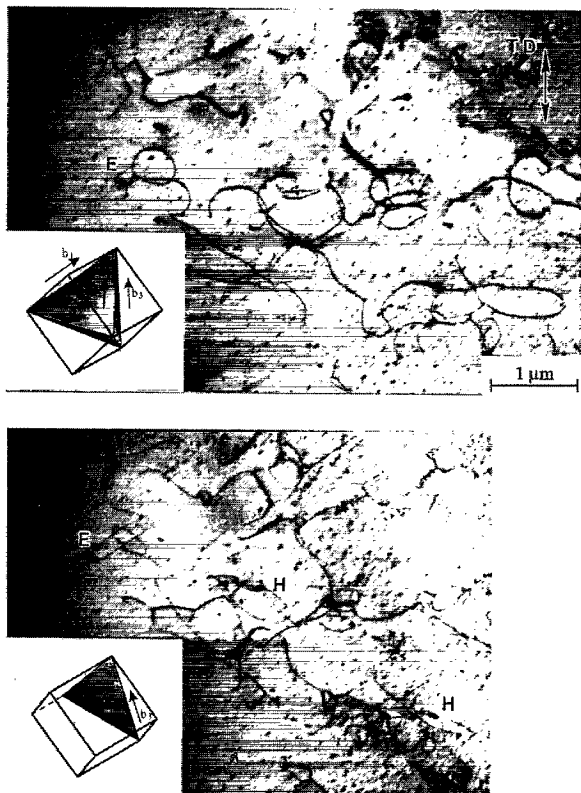

Fig. 4. Dislocation structure in a sample with (110) foil surfaces strained in situ in [1$\bar{1}$2] direction imaged at different zone axes. Post mortem investigation. (a) [110]; (b) [100].
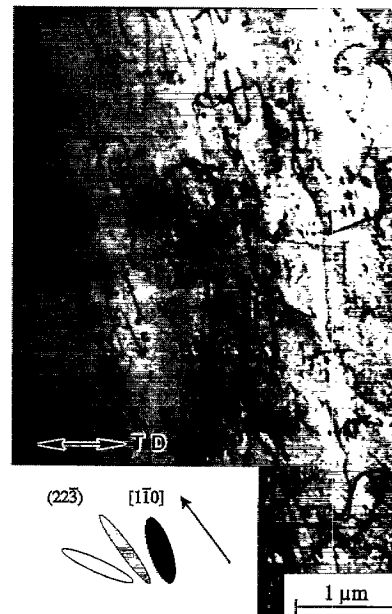

Fig. 5. Dislocation structure of the sample of Fig. 4 imaged at the [22$\bar{3}$] zone axis where the (211) plane is oriented nearly edge-on with respect to the foil surface. The insets represent projections of circular dislocation loops, which are arranged on the (111) plane (white), on the (011) plane (light grey) and on the (211) plane (black).
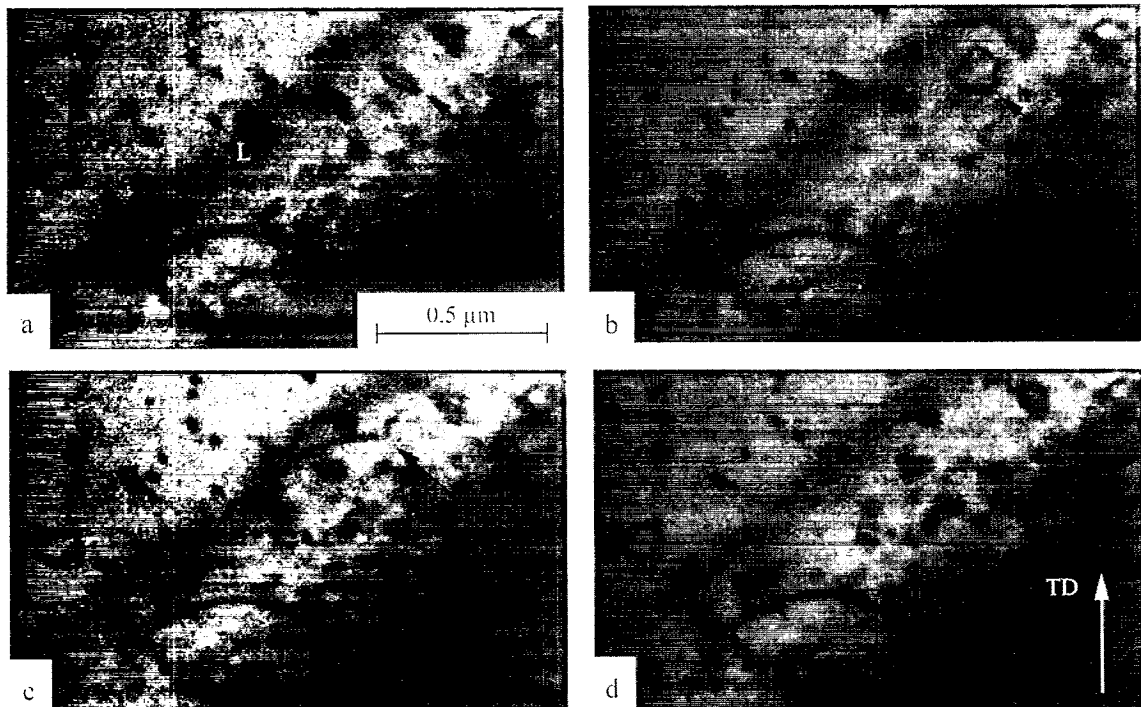
Fig. 6. Time sequence of a video recording during in situ straining in [1$\bar{1}$2] direction (TD) at 1150°C showing dislocation motion (marked by arrows) on the primary slip system. The moving dislocation escaped to the surface between (c) and (d) and the loop (L) between (a) and (b). The time interval between the micrographs was about 1 s.
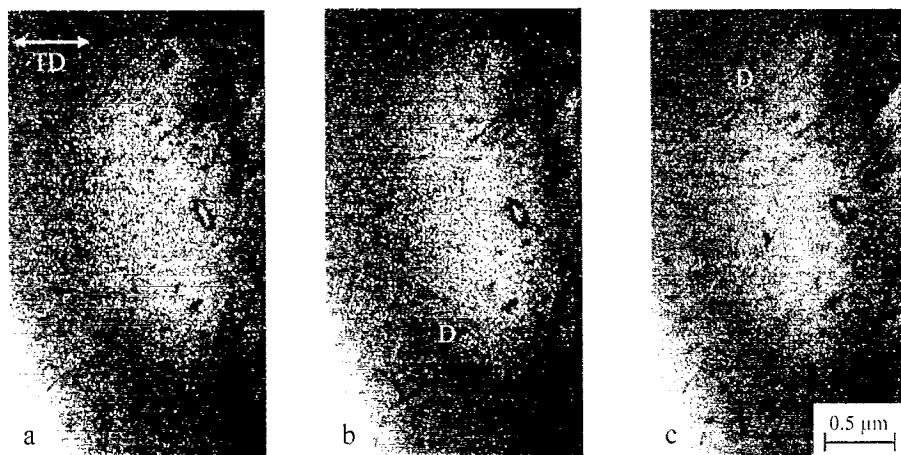

Fig. 7. Time sequence of a video recording obtained under the same conditions as in Fig. 6 which shows a dislocation (D) appearing between (a) and (b) and jumping between (b) and (c). [1$\bar{1}$2] Tensile direction (TD) and ($\bar{1}$11) foil surfaces.

In addition to their different configurations, the dislocations in the sample with (110) surfaces also showed quite a different dynamic behaviour. Sometimes the dislocations move jerkily, too, but the essential glide process observed during in situ experiments is almost continuous. Fig. 8 reveals the expansion of dislocation loops. The viscous glide of segments is shown in several micrographs of Fig. 9 taken at intervals of a few seconds. In Fig. 9(a)–(h), reproduced from a video sequence, both the viscous motion of dislocations and the jerky one of single segments are obvious. For

instance, loop A bows out continuously between Fig. 9(a) and (e), whereas dislocation B jumps to a new distant position, from one frame to the next. The motion between (c) and (d) of segment C is particularly marked. While most of the points where the dislocations emerge on the surface move in [1$\bar{1}$1] direction (horizontal direction in the micrographs), here the direction of motion is different. This also implies that more than one glide system is activated. The [1$\bar{1}$1] trace of the points of emergence may be assigned to the (01$\bar{1}$) slip plane. All {100} and {111} planes are not consis-
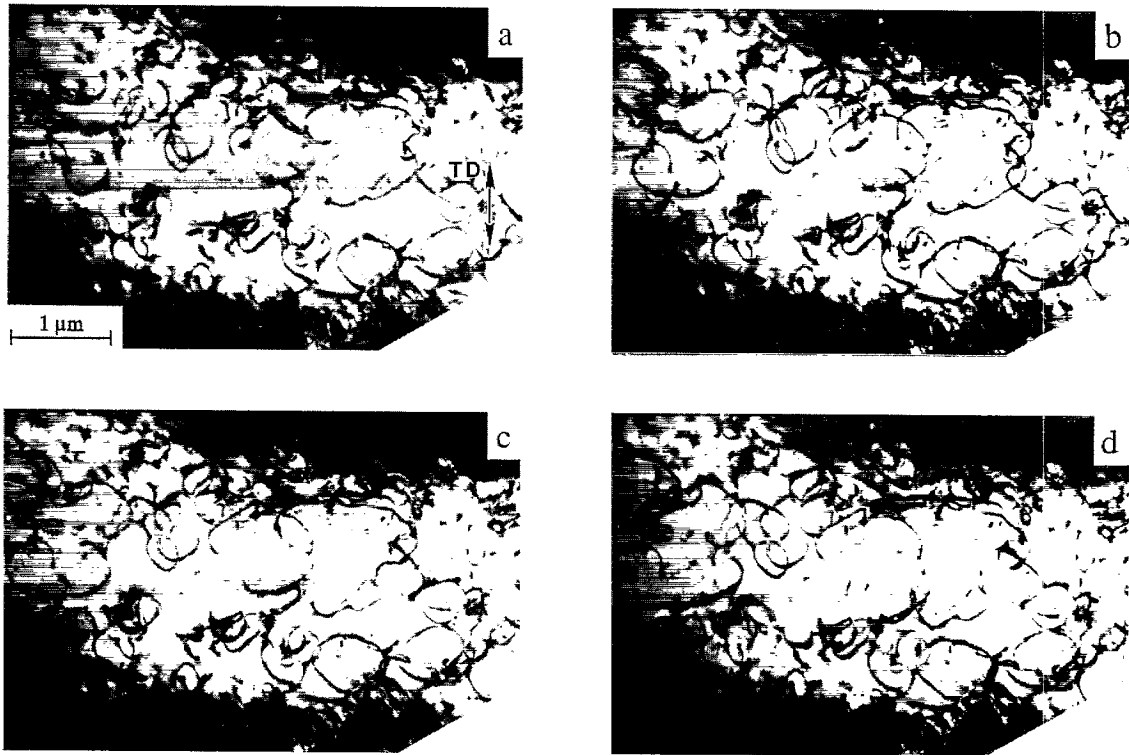
Fig. 8. Motion of dislocations during in situ straining in [1$\bar{1}$2] direction (TD) at 1150°C. (110) Foil surfaces. The micrographs are taken in time intervals of about 10 s.
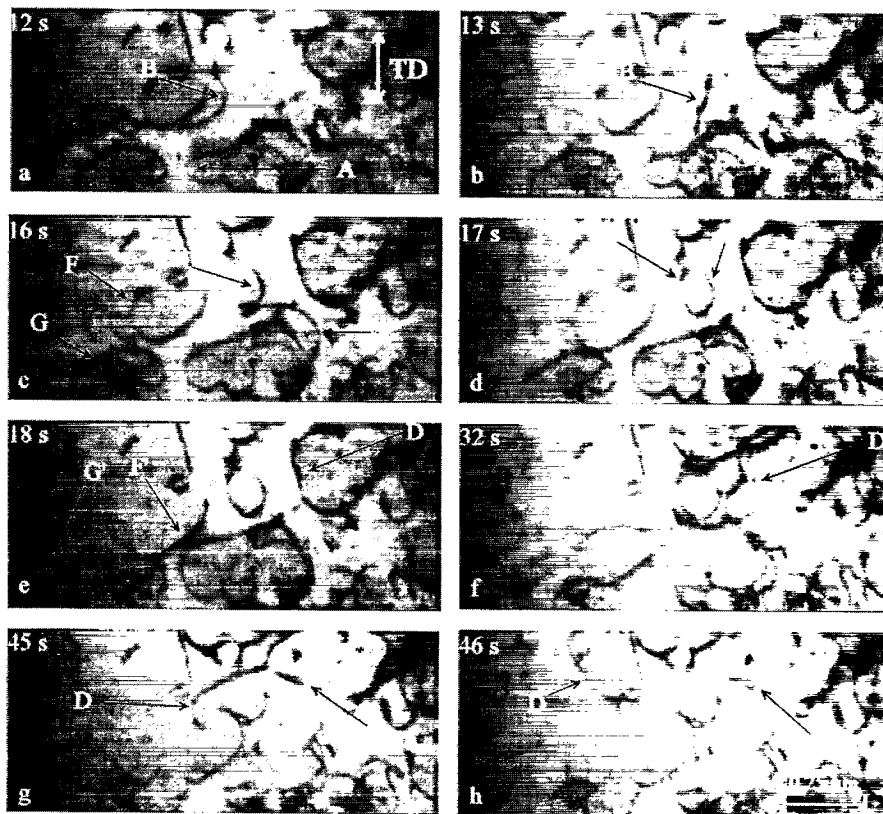

Fig. 9. Motion and interaction of dislocations in a video recording during in situ straining at 1150°C. [1$\bar{1}$2] Tensile direction (TD) and (110) foil surfaces. For explanation see text.
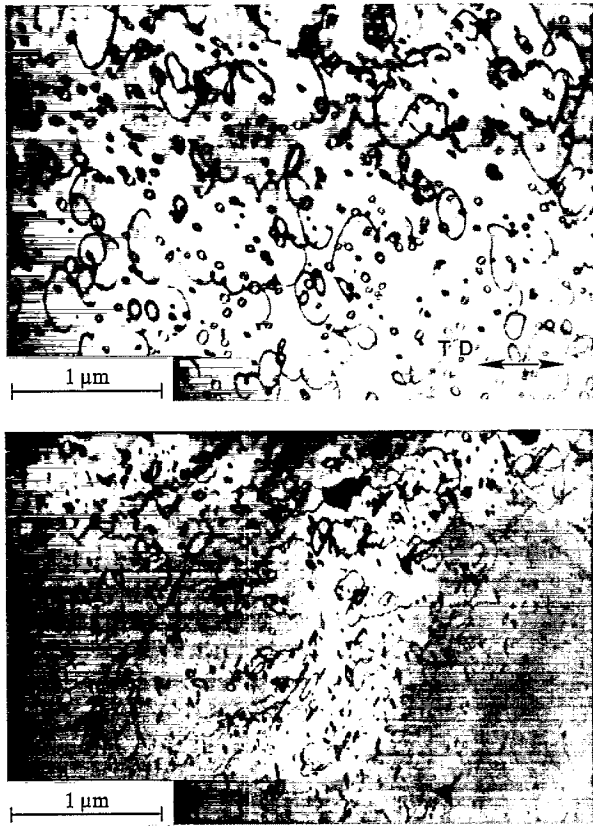
Fig. 12. Dislocation structure during in situ straining in [100] direction (TD) at 1150°C. Foil surfaces (001).

Fig. 10. Dislocations on the primary cube slip system, generated during straining of a specimen with ($\bar{1}$11) foil surfaces in [1$\bar{1}$2] direction (TD) at (a) 1150°C and (b) additional straining at 870°C.

tent with this trace. However, this (01$\bar{1}$) plane does not contain the Burgers vector of the dominating secondary slip system. As a low-index plane only the (211) plane

remains to give rise to the observed traces, thus confirming the result obtained from the tilting analysis.

Moreover, the sequence demonstrates the creation of a new dislocation loop E at dislocation D and the mutual annihilation of segments of dislocations F and G.

3.1.2. Deformation at 870°C

3.1.2.1. Dislocation structure.
One in situ straining experiment on a sample with ($\bar{1}$11) surfaces was started at 1150°C, then interrupted and continued at 870°C. Fig. 10(a) and (b) compare the initial dislocation structure created at 1150°C and its change during deformation at 870°C. The structures resemble each other, but after the temperature change the dislocation loops are much smaller and the screw dislocations are of curly shape. A large bending of the sample during the temperature

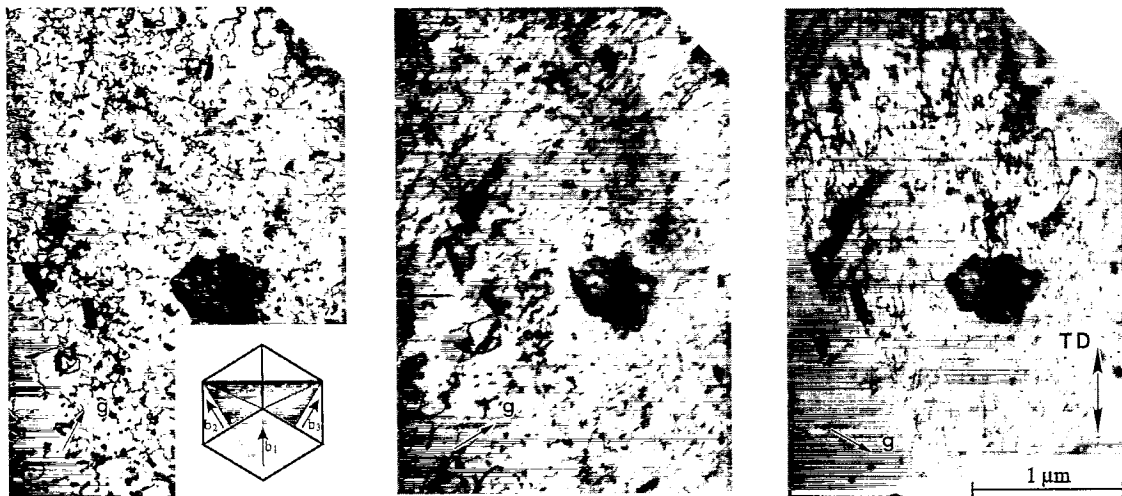Fig. 11. Post mortem micrographs of the sample shown in Fig. 10. (a) Dislocations of the primary cube slip system and those of a second cube slip system, which arose during deformation at 870°C. (b) The same specimen area taken with $\vec{g} = [200]$ at the [011] pole showing only the dislocations of the primary system. (c) Taken with $\vec{g} = [111]$ at the [$\bar{1}$10] pole showing those of the secondary system.
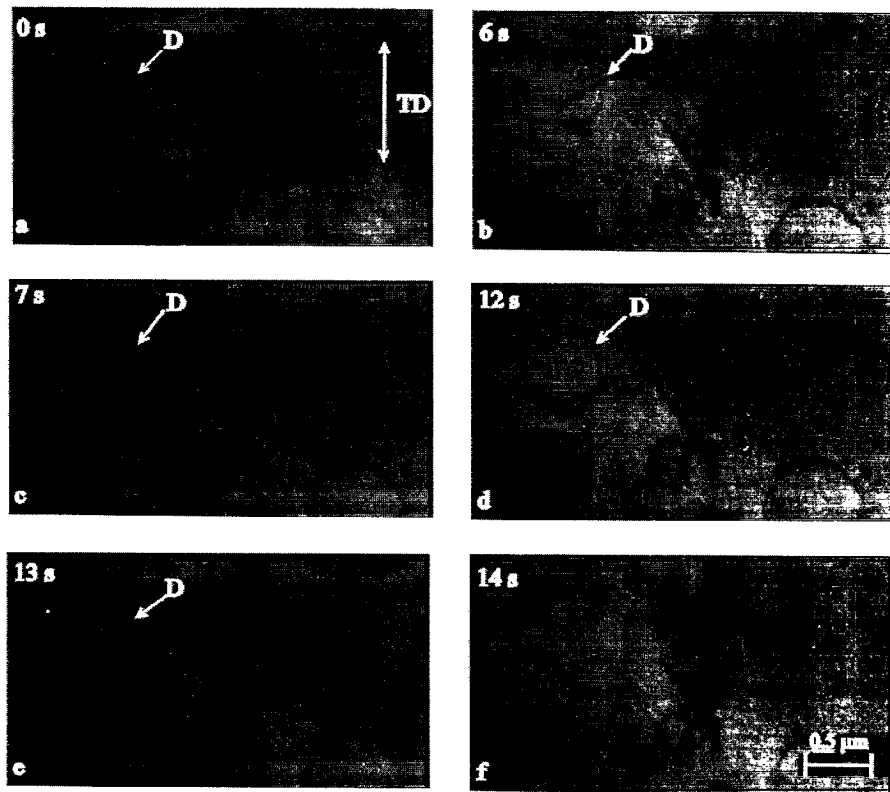
Fig. 13. Time sequence of a video recording during in situ straining in [100] direction (TD) at 1150°C showing the viscous motion of a dislocation D marked by arrows.

decrease caused considerable contrast variations. There-fore, the change of the shape of individual dislocations could not be investigated.

During low-temperature straining, a stress twice as large as that applied at 1150°C resulted in the develop-
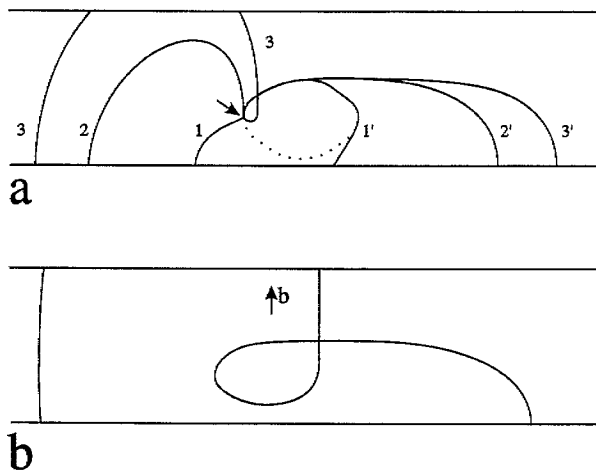

Fig. 14. Scheme of a single-ended source operating at a superjog. Successive stages of the operation. (a) The initial dislocation loop is drawn as a dotted line. Successive stages are named 1–3 or 1'–3', respectively. The prime indicates a different segment at the same stage. The anchoring point is marked by an arrow. (b) The relatively stable alpha-shaped dislocation configuration.

ment of a second dislocation band. In Fig. 11(a) both glide systems are imaged, whereas in Fig. 11(b) and (c) the dislocations of always one band are invisible. Fig. 11(b) taken near the [011] pole presents the bowed out dislocations of the primary slip system, and Fig. 11(c) taken near the [$\bar{1}$10] pole, the dislocations of the secondary system, which are preferentially in screw orientation. Extensive large-angle tilting experiments revealed that the glide plane of the secondary system is the (100) plane. This agrees with the macroscopic tests which indicate that the secondary [01$\bar{1}$](100) slip system is of the same type as the primary one.

3.1.2.2. Dislocation dynamics. The glide behaviour is similar to that observed at 1150°C i.e., the dislocations move jerkily, too, but their jump distances are shorter. Therefore, measuring the jump distances between the video frames was often successful, revealing a mean value of 0.3 μm resulting in a lower limit of the velocity during the jumps of 8 μm s^{-1}.

3.2. Deformation in ⟨100⟩ direction

For in situ straining in [100] direction samples were chosen with (001) foil surfaces. Two experiments carried out at 1150°C were successful. In [100] tensile direction the orientation factors for all cube planes are
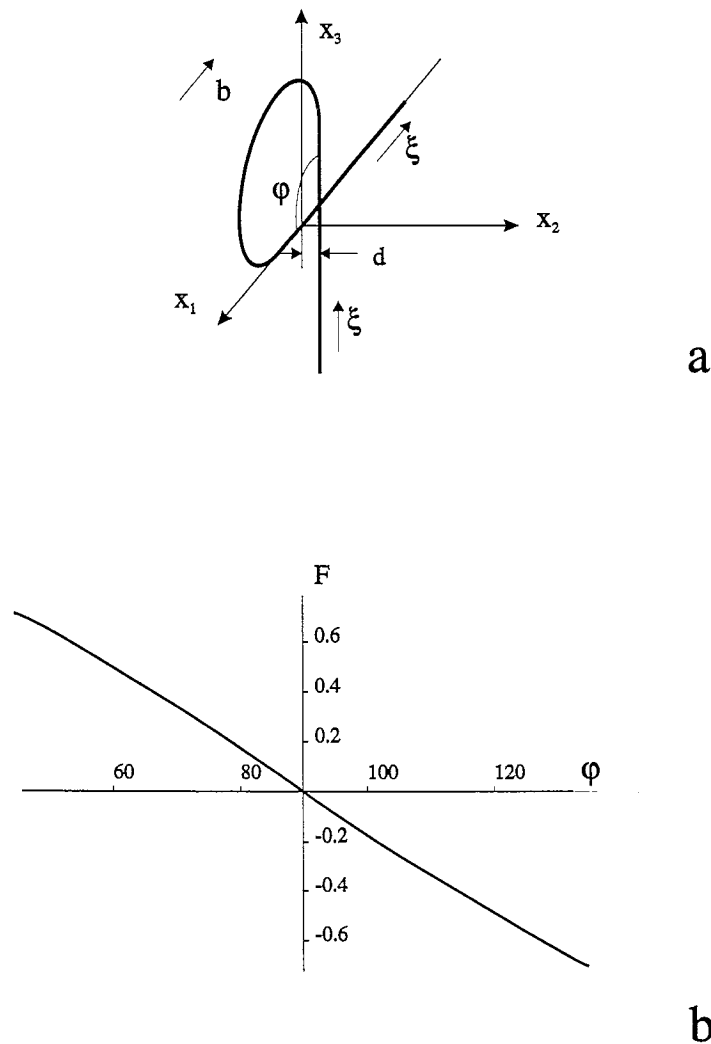
Fig. 15. Forces between dislocations on parallel slip planes. (a) Coordinate system and arrangement of the dislocations used for the calculation of the interaction force. The direction of the sessile dislocation is chosen parallel to $-x_3$ and the slip plane of the mobile dislocation is given by $x_1 - x_3$ at a distance d to the sessile dislocation measured in the direction of x_2. After Ref. [13]. (b) Force acting on the mobile dislocation perpendicular to its slip plane (x_2-direction) in dependence on its orientation.

zero, so that $\langle 1\bar{1}0\rangle\{111\}$ and $\langle 1\bar{1}0\rangle 110$ slip systems are expected to operate with orientation factors of 0.47 and 0.5, respectively. In both experiments, dislocations solely arose on the $\{101\}$ planes inclined to the foil surface. Fig. 12 shows an example of the typical dislocation structure, which in a large area does not appear as instantaneously as during $[\bar{1}1\bar{2}]$ deformation.

Dislocation glide proceeds rather continuously relative to $[\bar{1}1\bar{2}]$ deformation. In the video sequence of Fig. 13, the viscous behaviour is noticeable by the continuous expansion of the dislocation segment marked D within several seconds. Besides, at this anchored dislocation there are several steps of dislocation multiplication. The long edge segment in Fig. 13(b) emerged to the surface between Fig. 13(b) and (c), hence the screw segment remaining on the right has left the viewing range. Subsequently, the bowed-out segment expands

again, reaches the opposite surface in Fig. 13(e), with both resulting segments still visible.

It should be pointed out that in the figure, the points where the dislocations penetrate the surface move horizontally, i.e., in [010] direction, confirming the glide plane $\{101\}$ determined above.

4. Discussion

4.1. Dislocation multiplication

As is known from transmission electron microscopy (TEM) investigations of ZrO_2 specimens macroscopically deformed, the distance between the anchoring points along the dislocation lines is relatively large [4,5]. Therefore, associated with in situ deformation studies, the essential question arises as to which way dislocation
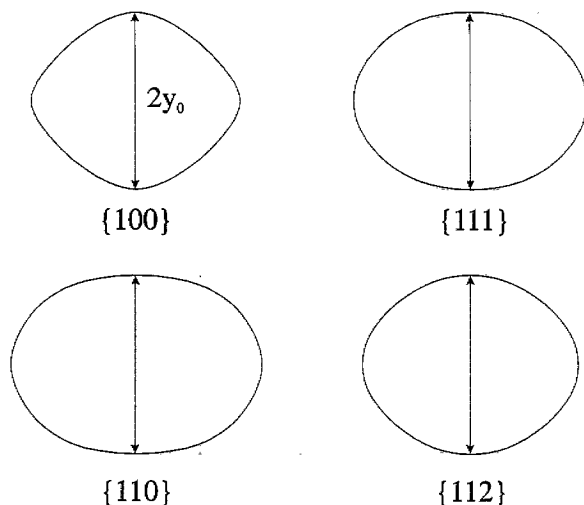
Fig. 16. Equilibrium shape of dislocation loops under load on different slip planes. Burgers vector $\vec{b} = 1/2\langle 110 \rangle$.

multiplication proceeds. Owing to the thin foil, a complex defect structure is restricted in its development and the dislocation segments may easily escape to the nearby surface after a short glide distance. Accordingly, single-ended sources may play the major role [11]. For the samples with $(\bar{1}11)$ surfaces, which were deformed in a $[\bar{1}1\bar{2}]$ direction, it is believed that the alpha-shaped structures represent a specific kind of single-ended sources. In contrast to well-known sources, where segments revolve round a superjog and emit dislocations [12], this source additionally punches out dislocation loops. The loops are nearly pure shear loops having only slight prismatic components. The particular behaviour of these sources results as the latter themselves arose from dislocation loops. If a dislocation loop expands, as shown schematically in Fig. 14(a), then an edge segment escapes to the foil surface at the given slip geometry. Assuming that in Fig. 14(a) a glissile screw segment is pinned to an anchoring point, i.e., a large
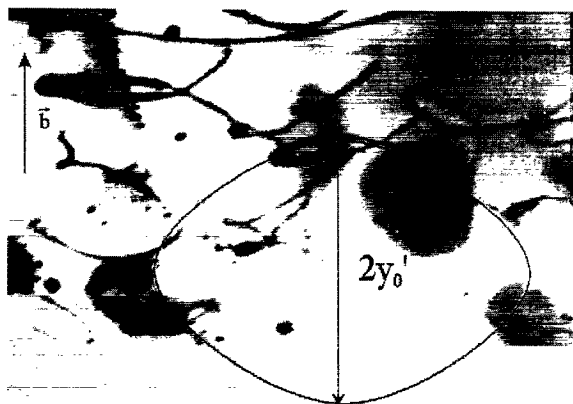

Fig. 17. Calculated loop on the {001} slip plane fitted to an observed dislocation segment.

jog, marked by the arrow, it revolves from stage 1 to stage 3, hence a screw dislocation is emitted. Up to this stage there is no general difference with respect to any pinned screw dislocation acting as single-ended source. However, if during further straining the screw segments of stages 3 or 3′, respectively, move rapidly, while the edge segment parallel to the surface remains relatively stable, the characteristic alpha-shaped structure develops. Here, a sufficiently large jog has to be presupposed so that the mobile segment is able to pass the stationary one. Specific features of the alpha-shaped structure are the preferred screw orientation of the glissile segment (3) and a relatively stable character of this configuration due to the less mobile edge segment. The screw character of segment (3) results from its tendency to attain an orientation perpendicular to the foil surface.

The features mentioned above are the prerequisite that a state can be attained where the glissile segment (3) is in perfect screw orientation at the cross-point between both dislocation segments. Then cross glide is possible. The segments may interact while pinching-off a relatively large loop, which lies almost parallel to the cube slip plane. A condition to be met if neighbouring segments should approach each other is that there are attractive forces between them. Fig. 15(a) shows the force acting on a glissile dislocation in the cross glide plane, depending on its orientation with respect to the stationary dislocation. The calculation was performed in accordance with the usual convention [13], where the x_3 axis is chosen parallel to the stationary dislocation and where, in the $x_1 - x_3$ plane, the mobile dislocation moves at distance d from the stationary one, measured in the direction of x_2 (see Fig. 15(b)). The cross-point between both dislocations is chosen as the origin, and the force is normalized to the distance d of the dislocations. It follows that the force is attractive for $\varphi < 90°$, i.e., the interaction is possible before the mobile segment has reached the edge segment lying parallel to the surface.

The specific nature of the alpha-shaped structure as a source for dislocation multiplication and its ability to pinch-off dislocation loops were attributed to the slip geometry with respect to the surface and the different mobility of edge and screw dislocations. The supposition of different mobilities is supported by the occurrence of numerous edge segments parallel to the surface at $(\bar{1}11)$ foil surfaces and the missing of adequate screw segments at (110) surfaces. This type of source is a dominating structure in foils with $(\bar{1}11)$ surface, where single slip is activated on the cube plane. Here, this source seems to affect deformation, because the created loop with its prismatic component may repeatedly start the described cycle, with the remaining dislocation exhibiting a large jog so that it may act as a usual single-ended source. In addition, the mechanism described above explains the large number of dislocation

loops in comparison with macroscopic deformation experiments, which are typical of these samples.

In samples strained in [100] direction, alpha-shaped structures appear, too. Owing to the viscous dislocation motion, even the intermediate stages of the pinch-off process of loops were recorded. As the alpha-shaped structures are arranged on the {101} planes inclined to the foil surface, the condition that the mobile dislocation segment exhibits preferred screw orientation is fulfilled, too. However, there seems to be no remarkable difference between the mobilities of edge and screw dislocations. Therefore, these structures occur only accidentally, thus being observed only in few cases.

A (110) foil surface instead of a $(\bar{1}11)$ one changes the generation of sources remarkably. During the expansion of loops on the primary glide system, the screw dislocations may easily emerge from the surface. Owing to their short glide distances the probability for cross glide and the formation of superjogs will be small. The remaining straight edge dislocations are not able to act as sources. Consequently, the generation of dislocations on the primary system is strongly restricted so that, unlike specimens with $(\bar{1}11)$ surfaces, only a few dislocation loops will arise on the primary system. As a consequence, further straining activates a secondary slip system, which was observed during in situ deformation. These secondary dislocations mostly wind around the straight primary edge dislocations (H in Fig. 4). A closer inspection reveals that they are pinned at a node. The node is part of a dislocation junction, which results from a reaction between the primary and the secondary dislocations according to $1/2[1\bar{1}1] + 1/2[01\bar{1}] = 1/2[10\bar{1}]$, and acts as the pinning agent of a source. As the primary dislocations have screw components relative to the glide plane of the winding secondary dislocations, the latter one winds into a conical helix around a 'pole' dislocation, which here is the edge dislocation of the primary system. Hence, the pitch of this helix equals the component of the Burgers vector of the pinning 'pole' dislocation perpendicular to the secondary glide plane [14]. It is not yet well understood why the helical-shaped dislocations are arranged on or near a (211) plane, although the orientation factor of 0.43 of this slip plane is larger than those of the (111) and (011) planes, amounting to 0.41 and 0.25, respectively.

4.2. Mechanisms controlling the flow stress

4.2.1. Back-stress of bowed-out dislocation segments

The curvature of the bowed-out dislocation segments is a measure of the local stress. This back-stress may considerably contribute to the flow stress. Within the framework of the line tension approximation [15,16], a relation between the local shear stress causing the bow-out of the segment and the curvature is given by:

$$\rho = \frac{E(\varphi) + (\mathrm{d}^2 E(\varphi)/\mathrm{d}\varphi^2)}{\tau_\mathrm{b} b} \tag{1}$$

or in a parametric form:

$$x = \frac{\sin \varphi E(\varphi) + \cos \varphi (\mathrm{d}E(\phi)/\mathrm{d}\varphi)}{\tau_\mathrm{b} b},$$

$$y = \frac{\cos \varphi E(\varphi) - \sin \varphi (\mathrm{d}E(\varphi)/\mathrm{d}\varphi)}{\tau_\mathrm{b} b} \tag{2}$$

Here, ρ is the local radius of curvature, E is the dislocation line energy as a function of angle φ between the line direction and the Burgers vector b, τ_b is the acting back stress or local shear stress and x, y are the Cartesian coordinates of the position of the dislocation line. Based on energy calculations for straight dislocations in anisotropic crystals, the formulae in Eq. (2) were used to determine the equilibrium shape for dislocation loops on {100}, {110}, {111} and {211} planes. The corresponding results are shown in Fig. 16. While the loops on the {100} plane show nearly straight segments preferentially in ⟨001⟩ orientation and on the {110} plane in screw orientation, the loop shapes for {111} and {211} planes very much resemble the elliptic shape obtained for isotropic crystals [17]. The preferred ⟨001⟩ orientation of loop segments on {100} planes was experimentally observed and described in Section 3.1.1 and can now be attributed to the anisotropic elasticity of the crystal having an anisotropy factor of [18]:

$$A = \frac{2C_{44}}{C_{11} - C_{12}} \approx 0.3$$

The actual local shear stress was estimated by projecting the calculated loops onto the viewing plane and by fitting them to the micrographs of the bowed-out dislocation segments, as demonstrated in Fig. 17. Then, the back stress τ_b is given by

$$\tau_\mathrm{b} = \frac{E(\varphi = 0)}{b y_0} \tag{3}$$

with $y_0 = y(\varphi = 0)$ being the half axis of the loop at the screw segment and considering that $\mathrm{d}E(\varphi = 0)/\mathrm{d}\varphi = 0$ and, therefore, $x(\varphi = 0) = 0$.

The values of $E(0)$ at 1150 and 870°C are 4.8×10^{-9} and 5.5×10^{-9} N, respectively. With the mean values of $y_0 \approx 0.2$ and 0.09 μm evaluated from the micrographs, one obtains local shear stresses of 75 ± 15 and 180 ± 30 MPa at 1150 and 870°C, respectively [6].

4.2.2. Deformation at 1150°C

In Sections 3.1.1 and 4, the occurrence of large jogs and their importance to dislocation multiplication were proven. The dislocations bow out between these large jogs. As obstacles to dislocation motion, they may be overcome solely by athermal processes like the formation of debris, i.e., the total activation energy is much be

supplied by the applied stress. Consequently, the back stress or local stress τ_b calculated from the curvature of the bowing segments contributes to the athermal stress component [7]. In addition, the long-range interactions between parallel dislocations essentially contribute to this athermal stress portion. The respective value resulting from a dislocation density of 2×10^{13} m^{-2} amounts to about 40 MPa [7]. This value together with the local shear stress of 75 MPa of the bowed-out segments and an orientation factor of 0.47 may explain the macroscopic flow stress $\sigma = 250$ MPa. Thus, the estimation confirms that contributions to the flow stress resulting from thermally activated processes are negligible in this temperature range in agreement with the conclusion drawn from the very small values of the strain rate sensitivity in macroscopic stress relaxation experiments [6,7]. The above result is also in accordance with the dynamic behaviour of dislocations in the present in situ experiments proving their very jerky motion on the cube planes.

At a first glance, the present results are at variance with the stress dependence of the dislocation velocity measured by the stress pulse etching technique in the same temperature range [19]. These measurements cover a stress range between 60 and 180 MPa, i.e., below the macroscopic flow stress. At higher stresses, dislocation velocities could not be determined because of rapid dislocation multiplication. Similarly, the velocities reached at these low stresses are very low so that unreasonably high densities of mobile dislocations are necessary to explain macroscopic deformation rates. The stress exponent between 1 and 2 at 1150°C, which is not compatible with athermal dislocation motion, is much lower than that of the order of magnitude of 200 following from the very low strain rate sensitivity in macroscopic experiments. It has to be considered, however, that the microstructure of the crystals in Ref. [19] greatly differs from that in the present study. The dislocation density in the macroscopic tests as well as in the in situ experiments is two to three orders of magnitude higher than the grown-in dislocation density during the velocity measurements. Therefore, long-range stresses of other dislocations only slightly influence the dislocation velocity measurements, whereas they are the main obstacle to dislocation motion in macroscopic experiments. It has to be ascertained quantitatively whether the velocity data for the relatively high temperatures above 1100°C are compatible with the Peierls mechanism certainly operating on cube planes at temperatures below 500°C [7].

On non-cube slip planes, however, the more continuous or viscous motion at 1150°C should be attributed to a lattice friction mechanism, like the Peierls mechanism. This result is consistent with a critical flow stress on these planes, which is about twice as high as that on cube planes [8].

4.2.3. Deformation at 870°C

The very curly shape of the dislocations in this temperature range is interpreted as a strong localized pinning, which causes a large increase of the flow stress at low temperatures. The nature of these pinning points has not been identified, but it is assumed that most of them are localized obstacles, i.e., probably small precipitates. This assumption also follows from the increased strain rate sensitivity measured in macroscopic deformation tests, which can be explained by the thermally activated overcoming of localized obstacles [5,14,15]. In addition, the in situ experiment at this temperature confirmed that the critical resolved shear stress for the cube slip system is distinctly lower than that for {111} planes, as a second cube system with an orientation factor of 0.35 was activated instead of the $\langle 1\bar{1}0 \rangle 111$ system with an orientation factor of 0.41.

5. Conclusions

The in situ straining experiments yielded selective structural and dynamic information on the slip systems in cubic zirconia. The activation of different slip systems at 1150°C as function of the orientation of the tensile axis and the foil surfaces was mainly attributed to the mode of dislocation multiplication. Dislocations on different slip systems show a very different dynamic behaviour. On cube planes, they move very jerkily, i.e., their motion is controlled by athermal long-range interactions between dislocations (τ_i). However, the smooth viscous motion on non-cube planes should be caused by the action of a lattice friction mechanism. The local shear stress τ_b, which was estimated from the curvature of dislocation segments bowing out between high jogs, corresponds to a material under load. The local shear stress τ_b together with τ_i caused by the long-range interactions may explain the flow stress measured in macroscopic tests. Thus, a semi-quantitative understanding of the glide process for single slip on the primary cube system was achieved. Contrary to this, the dislocation structures observed after macroscopic experiments are always relaxed, even if cooled under load, and yield too small stress values.

At 870°C the in situ experiments confirmed the precipitation hardening model, which was derived from macroscopic experiments and conventional transmission electron microscopy.

References

[1] D.S. Cheong, A. Dominguez-Rodriguez, A.H. Heuer, Philosophical Magazine A 60 (1989) 123.

[2] D.S. Cheong, A. Dominguez-Rodriguez, A.H. Heuer, Philosophical Magazine A 63 (1991) 377.

[3] A. Dominguez-Rodriguez, D.S. Cheong, A.H. Heuer, Philosophical Magazine A 64 (1991) 923.

[4] A. Dominguez-Rodriguez, K.P.D. Lagerloef, A.H. Heuer, Journal of the American Ceramics Society 69 (1986) 201.

[5] B. Baufeld, M. Bartsch, U. Messerschmidt, D. Baither, Acta Metallurgica et Materialia 43 (1995) 1925.

[6] B. Baufeld, Ph.D. Thesis, Halle (Saale), Germany, 1996.

[7] U. Messerschmidt, B. Baufeld, D. Baither, in: E. Kisi (Ed.), Zirconia Engineering Ceramics: Old Challenges–New Ideas, Key Engineering Materials, Trans. Tech. Publications, Switzerland, (in press).

[8] B. Baufeld, U. Messerschmidt, D. Baither, M. Bartsch, A. Foitzik, M. Rühle, in: R.C. Bradt, C.A. Brockes, J.L. Routbart (Eds.), Plastic Deformation of Ceramics, Plenum Press, New York, 1993, p. 43.

[9] U. Messerschmidt, B. Baufeld, D. Baither, M. Bartsch, in: S. Meriano, V. Sergo (Eds.), 4th Euroceramics, Vol. 3, Gruppo Editoriale Faenza Editrice, 1995, p. 479.

[10] U. Messerschmidt, M. Bartsch, Ultramicroscopy 56 (1994) 163.

[11] L.P. Kubin, F. Louchet, D. Caillard, J.L. Martin, in: T. Imura (Ed.), Electron Microscopy, Vol. 4, 1980, p. 288.

[12] C.B. Carter, Philosophical Magazine 35 (1977) 75.

[13] R. Bullough, J.V. Sharp, Philosophical Magazine 11 (1965) 605.

[14] J.P. Hirth, J. Lothe, Theory of Dislocations, Wiley-Interscience, New York, 1982, p. 755.

[15] G. DeWitt, J.S. Koehler, Physics Review 116 (1959) 1113.

[16] D.M. Barnett, R.J. Asaro, S.D. Gavazzi, D.J. Bacon, R.O. Scattergood, Journal of Physics F: Metal Physics 2 (1972) 854.

[17] U. Messerschmidt, F. Appel, Kristall und Technik 14 (1979) 1331.

[18] P.J. Botha, J.C.H. Chiang, J.D. Comins, P.M. Mjwara, P.E. Ngoepe, Journal of Applied Physics 73 (1993) 7268.

[19] B.Y. Farber, A.S. Chiarelli, A.H. Heuer, Philosophical Magazine A 72 (1995) 59.